Acta Mech. Sin. (2012) 28(2):1–13
DOI 10.1007/s10409-012-0035-5

RESEARCH PAPER

A numerical study of fluid injection and mixing under near-critical conditions

Hua-Guang Li · Xi-Yun Lu · Vigor Yang

Received: 25 June 2011 / Revised: 2 November 2011 / Accepted: 10 November 2011

Abstract Nitrogen injection under conditions close vicinity of the liquid-gas critical point is studied numerically. The fluid thermodynamic and transport properties vary drastically are highly variable and exhibit anomalies in the near-critical regime. These anomalies can cause distinctive effects on heat-transfer and fluid-flow characteristics. To focus on the influence of thermodynamics on the flow field, a relatively low injection Reynolds number of 1 750 is adopted. For comparisons, a reference case with the same configuration and Reynolds number is simulated in the ideal gas regime. The model accommodates full conservation laws, real-fluid thermodynamic and transport phenomena. Results reveal that the flow features of the near-critical fluid jet are significantly different from their counterpart. The near-critical fluid jet spreads faster and mixes more efficiently with the ambient fluid along with a more rapidly development of the vortex pairing process. Detailed analysis at different streamwise locations including both the flat shear-layer region and fully developed vortex region reveals the important effect of volume dilatation and baroclinic torque in the near-critical fluid case. The former disturbs the shear layer and makes it more unstable. The volume dilatation and baroclinic effects strengthen the vorticity and stimulate the vortex rolling up and pairing process.

Keywords Liquid-gas critical point · Real-fluid · Fluid injection · Shear layer instability · Vortical dynamics

The project was supported in part by the National Natural Science Foundation of China (11132010 and 11072236).

H.-G. Li · X.-Y. Lu (✉)
Department of Modern Mechanics,
University of Science and Technology of China,
230026 Hefei, China
e-mail: xlu@ustc.edu.cn

V. Yang
School of Aerospace Engineering,
Georgia Institute of Technology,
Atlanta, GA 30332, USA
e-mail: vigor.yang@aerospace.gatech.edu

1 Introduction

When approaching the liquid-gas critical point, thermodynamic and transport properties of a fluid exhibit anomalies [1]. For example, the isothermal compressibility and volume expansion coefficient diverge and become orders of magnitude higher than those at the standard states. Thermal diffusivity tends to diminish due to the diverging specific heat under constant pressure, and the kinetic viscosity becomes very small due to the large density. Figure 1 shows the situation with nitrogen in the vicinity of the critical point, $T_{\rm cr} = 12.62$ K, $P_{\rm cr} = 3.4$ MPa. With diverging isothermal compressibility and volume expansion coefficients, a small change of pressure or temperature can induce a large density variation. At the critical point pressure, a more than 50% density reduction of nitrogen fluid occurs when the temperature increases 1 K from the critical value, whereas 1 K temperature increase can only induce less than 0.5% of density variation at the standard state. The thermal diffusion coefficient of near-critical nitrogen at ($T_{\rm cr}$ + 1 K, $p_{\rm cr}$) is more than three orders of magnitude lower than that of gas nitrogen at the standard state.

Dramatically varied properties of a near-critical fluid have significant impacts on fluid dynamics, heat transfer, chemical reaction and phase transition. A low thermal diffusion hinders heat transfer and causes slow down of thermal equilibration. High compressibility significantly affects the mechanical response of fluid to thermal disturbance. Under conditions close to the critical point, a locally heated fluid can expand considerably and cause strong compression waves which further compress and heat the rest of the fluid homogeneously in a short time. Such fast thermalization process leading to critical speeding up of thermal equilibrium is known as the piston-effect. Zappoli et al. [2], Boukari et al. [3] and Onuki et al. [4] examined the key role of high compressibility and slow heat diffusion in the piston effect by means of numerical simulation of one-dimensional side heated near-critical fluid. Wagner [5] conducted a similar study using both the van der Waals equation of state and a more accurate equation of state obtained from the National

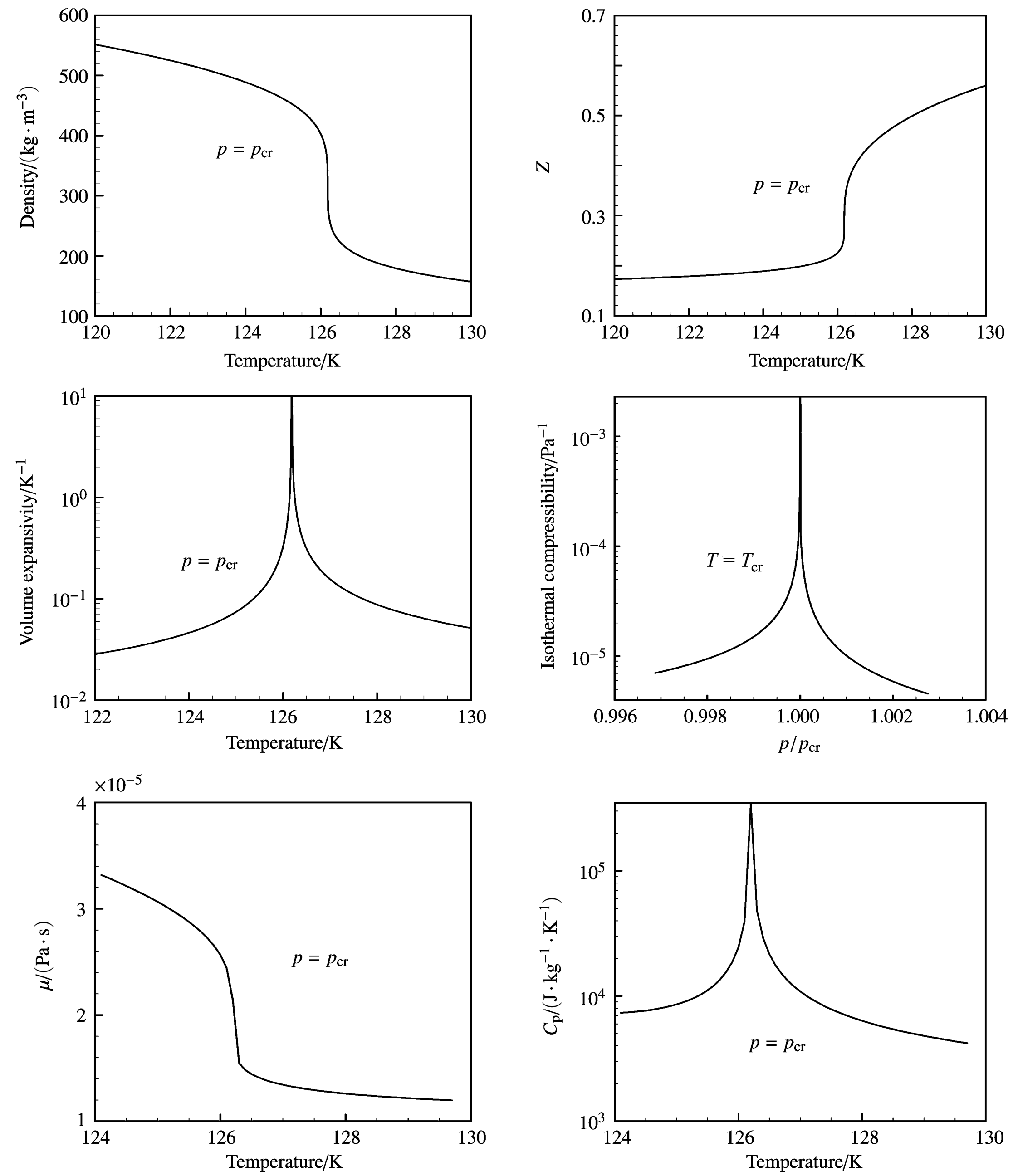

Fig. 1 Thermodynamic and transport properties of nitrogen in the close vicinity of the critical point

Institute of Standard and Technology (NIST). The necessity of using accurate equations of state for treating drastically varied near-critical fluids was thereby demonstrated. Frohlich et al. [6] performed experiments to study the piston-effect induced thermal jet for fluids at near-critical conditions. The role of heated boundary-layer expansion was investigeted in dictating the flow evolution. Zappoli [7] further studied center-heated two-dimensional square cavity flows containing CO_2 at either near-critical and ideal-gas conditions. The buoyancy greatly affects the near-critical fluid flow and leads to a very different flow pattern from the ideal-gas case. In addition to the above fundamental studies, near-critical fluids were used in a reduced scale model for treating internal gravity waves in geophysical research [8]. The reason is that near-critical fluids can form strong stratification in a short distance under its own weight. In spite of many different aspects of drastically varied near critical fluid flows, the current work mainly focuses on fluid-dynamics and heat-transfer characteristics.

Extensive work has been conducted to investigate fluid injection at standard state. For a constant density laminar jet, the flow structure depends mainly on the injection Reynolds number [9, 10]. The jet spreading behavior is determined by the instabilities of shear layers between the jet and ambient fluid. Vortices roll up at the fundamental frequency of the shear layer instability. The vortex pairing process that happens in the downstream region leads to sub-harmonic low frequency oscillations. Compared with a high Reynolds number turbulent jet, a low Reynolds number laminar jet has a larger spreading rate and more intensive entrainment due to dominance of larger flow structures. When the injection Reynolds number is larger than a certain value, the jet spreading rate tends to level off and becomes independent of the Reynolds number [9]. For a variable density jet, when the jet density is higher than its ambient fluid counterpart, the density stratification between the jet and ambient fluid has a stabilization effect on the shear layer. The larger the density gradient is, the more stable the shear layer and the smaller the spreading rate is [11]. If the jet density is lower, the jet spreading rate and instability behavior of jet are no longer determined by the behavior of the shear layer, and absolute instability is developed in the core region. Vortices roll up at a frequency is different from the basic frequency of shear layer instability. Instead, the frequency is determined by the jet dimension and the density gradient. It is an intrinsic characteristic of a low density jet, similar to the Karman vortex street in a flow passing over a cylinder [12, 13].

Substantial efforts have also been made to study fluid injection in high pressure environment [1]. Newman and Bizustowski [14] studied injection of liquid CO_2 into a chamber containing a gas mixture of N_2 and CO_2 under the near-critical conditions of CO_2. It was observed that considerable change in the jet surface takes place at near-critical pressures and significantly influences the atomization process. Akira and Yuichro [15] conducted microgravity experiments of liquid SF_6 injection into N_2 gas at a near-critical state of SF_6. A maximum growth rate proportional to the relative velocity was achieved and an instability, neither the Rayleigh instability nor the Taylor instability, was observed. Oschwald [16] and Chehroudi [17, 18] conducted experiments of fluid injection in both subcritical and supercritical environments. The results show that the supercritical fluid jet behaves like variable density gas jets while atomization process appear in the subcritical fluid jet.

Bellan and colleagues [19, 20] examined temporal evolution of heptane/nitrogen and oxygen/hydrogen mixing layers at supercritical conditions. They identified the stabilization role of density gradient in shear layers and the prevalent effects of species and heat fluxes in energy dissipation. Zong and Yang [11] conducted comprehensive analysis of cryogenic fluid injection and mixing under supercritical conditions using a treatment of numerical algorithm based on general thermodynamics. It was found that the jet dynamics depend highly on the local fluid thermodynamic state especially when the temperature transits across the inflection point in an isobaric process. The frequency of the most unstable mode decreases significantly in the near-critical regime due to the enhanced effect of density stratification and increased mixing layer momentum thickness. Oefelein et al. [21, 22] and Zong et al. [23, 24] numerically studied combustion of chemically reacting shear flows under supercritical conditions.

Both constant and variable density jets at standard state and in supercritical environments have been studied extensively. Much less attention, however, is given to fluid injection under conditions very close to the critical point. Considering the anomalies of near-critical fluid properties, it is inconvincible to extend the results and theories for regimes away from the critical point to those in the close vicinity of the critical point. The object of the present work is to study the near-critical fluid injection and to explore the influence of drastically varied properties of near-critical fluids on heat transfer and flow characteristics.

2 Theoretical formulation

The formulation is based on the conservation equations of mass, momentum and energy

$$\frac{\partial \rho}{\partial t} + \frac{\partial \rho u_j}{\partial x_j} = 0, \tag{1}$$

$$\frac{\partial \rho u_i}{\partial t} + \frac{\partial (\rho u_i u_j + p\delta_{ij})}{\partial x_j} = \frac{\partial \tau_{ij}}{\partial x_j}, \tag{2}$$

$$\frac{\partial \rho E}{\partial t} + \frac{\partial ((\rho E + p) u_i)}{\partial x_i} = \frac{\partial}{\partial x_i}\left(u_j \tau_{ij} + q_i\right), \tag{3}$$

where ρ, u_i, p, E, τ_{ij} and q_i represent the density, velocity components, pressure, specific total energy, viscous stress tensor and heat flux, respectively.

The equation of state is important for high-pressure real-fluid flow simulations, especially for near-critical fluids with steep property variations. Cubic equations of state are most popular in supercritical fluid simulations due to its easily implementation and less calculation cost. They are, however, less accurate than the Benedict-Webb-Rubin (BWR) equation of state in the near-critical regime [1]. Although much more computation time is required for the BWR equation of state, for accuracy it is employed in the present study, taking the following form

$$p = \sum_{n=1}^{9} A_n(T)\rho^n + \sum_{n=10}^{15} A_n(T)\rho^{2n-17}\, \mathrm{e}^{-\gamma\rho^2}, \tag{4}$$

where A_n are the coefficients given in detail by Jacobsen and Stewart [25].

Thermodynamic properties, such as enthalpy, internal energy and constant pressure specific heat, can be expressed as the sums of ideal-gas properties at the same temperature and departure functions which take into account the dense-fluid correction [1],

$$e(T,\rho) = e_0(T) + \int_{\rho_0}^{\rho} \left[\frac{p}{\rho^2} - \frac{T}{\rho^2}\left(\frac{\partial p}{\partial T}\right)_\rho\right]_T \mathrm{d}\rho, \tag{5}$$

$$h(T,p) = h_0(T) + \int_{P_0}^{P} \left[\frac{1}{\rho} + \frac{T}{\rho^2}\left(\frac{\partial \rho}{\partial T}\right)_P\right]_T \mathrm{d}p, \tag{6}$$

$$C_P(T,\rho) = C_{V0}(T) - \int_{\rho_0}^{\rho}\left[\frac{T}{\rho^2}\left(\frac{\partial^2 p}{\partial T^2}\right)_\rho\right]_T \mathrm{d}\rho + \frac{T}{\rho^2}\left(\frac{\partial p}{\partial T}\right)_\rho^2 \Big/ \left(\frac{\partial p}{\partial \rho}\right)_T, \tag{7}$$

where the subscript "0" refers to the ideal state at low pressure. The departure functions on the right-hand sides of Eqs. (5)–(7) can be determined from the equation of state.

Transport properties including viscosity and thermal conductivity are estimated by means of the corresponding state principles along with the 32-term BWR equation of state [1]. Figure 1 shows the compressibility factor, specific heat, viscosity, and thermal conductivity of nitrogen in the close vicinity of the critical point. These figures illustrate key trends over the range of pressure and temperature of interest. With a slight temperature increase of 1K from $T_{\rm cr}$ + 0.1 K. The density decreases about 20%, and the thermal diffusivity increases five times, the volume expansion and the isothermal compressibility coefficient decrease by one order of magnitude. For nitrogen at $T_{\rm cr}$ + 0.1 K, $p_{\rm cr}$, the thermal diffusivity and kinetic viscosity is four and three orders smaller than its counterpart of gas at standard state, respectively. The volume expansion and isothermal compressibility coefficient is three and one order of magnitude higher than that of gaseous nitrogen at standard state, respectively.

3 Numerical methods

To overcome the stiffness problem caused by rapid variations of fluid properties and wide disparities in the characteristic time scales, an efficient preconditioning scheme developed by Meng and Yang [26] and Zong and Yang [27] for real-fluid compressible flows is adopted here

$$\boldsymbol{\Gamma}\frac{\partial \widehat{\boldsymbol{Q}}}{\partial \tau} + \frac{\partial \boldsymbol{Q}}{\partial t} + \frac{\partial(\boldsymbol{E}-\boldsymbol{E}_v)}{\partial x} + \frac{\partial(\boldsymbol{F}-\boldsymbol{F}_v)}{\partial y} = \boldsymbol{0}, \tag{8}$$

where $\boldsymbol{\Gamma}$ represents the preconditioning matrix. t is the real time and τ the pseudo-time. $\boldsymbol{Q}$ is the conservative variable vector and $\widehat{\boldsymbol{Q}}$ primitive variable vector.

$$\widehat{\boldsymbol{Q}} = (p', u, v, w, T, Y_1)^{\rm T}, \tag{9}$$

$$\boldsymbol{Q} = (\rho, \rho u, \rho v, \rho w, \rho e_t, \rho Y_1)^{\rm T}, \tag{10}$$

$\boldsymbol{E}, \boldsymbol{F}$ are convective fluxes and $\boldsymbol{E}_v, \boldsymbol{F}_v$ viscous fluxes in the x-, y-direction, respectively. The scalar variable Y_1, equal to 1 for pure injected fluid and 0 for ambient fluid, presents the distribution of the injected fluid. The pressure is decomposed into a constant reference pressure p_0 and a gauge pressure p' to circumvent the pressure singularity problem at low Mach numbers [28].

$$p = p_0 + p'. \tag{11}$$

A density-based cell-center type finite volume method is used to discretize the governing equations. A fourth-order central difference algorithm in generalized coordinates is employed for spatial discretization. Second- and fourth-order artificial dissipation with a total variation diminishing switch developed by Swanson and Turkel [29] is implemented to ensure computational stability and prevent numerical oscillations in regions with steep gradients. Temporal discretization is obtained using second order backward difference, and the inner-loop pseudo-time term is integrated with a third-order Runge-Kutta scheme. Multi-block domain decomposition technique along with static load balance is employed to facilitate the implementation of parallel computation with message passing interfaces at the domain boundaries. This approach has been extensively validated by Nan and Yang [11, 27], Meng and Yang [26].

4 Configuration and boundary conditions

The physical configuration and computational domain studied are shown in Fig. 2. The injector width D_j is set to 0.25 mm and its length is $4D_j$. The computational domain downstream of the injector measures a length of $40D_j$ and a width of $6D_j$. The entire grid system consists of 280 and 120 points along the streamwise and vertical direction, respectively. The grids are clustered in the shear layer and near the injector to resolve the rapid property variations.

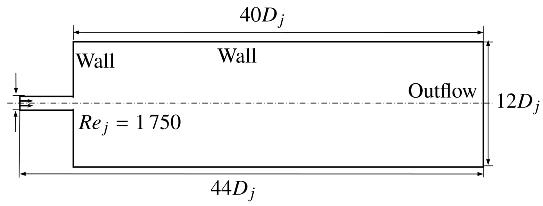

Fig. 2 Schematic of numerical simulation model

At the injector inlet, the velocity follows the one-seventh-power law and temperature is specified with a top-hat profile. The pressure is determined by using a one dimensional approximation to the momentum equation in the axial direction. At the downstream outlet boundary, the non-reflecting boundary conditions proposed by Li et al. [30] are adopted applied to avoid undesired reflection of compression and expansion waves propagating into the computational domain. The non-slip and adiabatic conditions are enforced along the solid walls. Only the upper half is considered and symmetric boundary conditions are used at the center line of the domain.

For comparison, a near-critical fluid jet and an ideal gas jet with the same injection Reynolds number of 1 750 are treated. The same critical pressure of nitrogen $p_{\rm cr}$ is adopted for the two cases considered. The fluid temperature is set to $T_{\rm cr}$ + 0.1 K for the near-critical fluid case and 500 K for the ideal gas case. Detailed flow parameters are listed in Table 1.

Table 1 Parameters of cases modeled: near-critical fluid jet and ideal gas jet at critical point pressure of nitrogen $p_{\rm cr}$ (β_p is isothermal compressibility; γ_T is volume expansivity; Z is compressive factor)

T/K	β_p/K^{-1}	γ_T/(m$^2\cdot$s^{-1})	Z	Ma
$T_{\rm cr}+0.1$	0.73	2.24×10^{-9}	0.37	2.9×10^{-3}
500	2.0×10^{-3}	1.63×10^{-6}	1.00	2.0×10^{-2}

5 Results and discussion

5.1 Instantaneous flow fields

The flow structures are characterized by convection, diffusion and density stratification between the injected fluid and the ambient fluid. The flow behaviors depend mainly on the injection Reynolds numbers for a constant density jet. The Reynolds number for both near-critical and ideal gas cases are chosen the same, $Re_j = \rho_j u_j D_j/\mu_j = 1\,750$, where the subscript "$j$" represents quantities of the injected fluid. With the same Reynolds number, injector width, initial pressure and different temperature, different Mach numbers are obtained, i.e. 2.9×10^{-3} for the near-critical fluid case and 2.0×10^{-2} for the ideal gas case. Since the Mach number is very small, it may not induce obvious difference between the two cases.

The instantaneous flow fields exhibit different flow behaviors between the two cases. The fluid is injected from the injector into an initially stationary flow field in the chamber. Compression waves are generated in the chamber from the dynamic pressure of the injected fluid. Similar to the piston-effect, the temperature and pressure of fluid in the chamber enhanced after the compression wave passing. The fluid in the chamber is heated in a short time before the injected fluid enter the chamber. Since the injection Mach number is very low, the density variation induced by the pressure change is less than 0.01%. On the other hand, the temperature variation has a dominant effect on the density change. For the ideal gas case, the magnitude of temperature increase in the chamber is 0.8% and the density decrease 0.2%, while the temperature increase of near-critical fluid case is 0.03% and the density decrease 4%. With smaller temperature variation, larger density change occurs in the near-critical fluid case due to the larger volume expansion coefficient.

For a constant density jet, the shear layer between the jet and the ambient fluid is susceptible to the Kelvin-Helmholtz instability and experiences vortex rolling, paring and breakup. Near-critical fluid jet undergoes qualitatively the similar process but with additional mechanisms arising from volume dilatation and baroclinic torque. Figure 3 shows the snapshots of the marking scalar Y_1, vorticity magnitude $|\omega|$, density ρ and density gradient $|\nabla\rho|$ for both the cases. After the flow field achieves a stationary state, the temperature difference between the injected fluid and ambient fluid still exists, but the piston-effect is no longer obvious as that in confined fluids due to the half open configuration. The fluid expansion induced by the thermal disturbance, however, still has an important effect on the flow field evolution, which will be discussed in the following sections. The near-critical fluid jet is more unstable compared to the ideal gas jet. In the near-critical fluid case, the shear layer has shorter stable section before vortex rolling up. The larger vortex structure in the near-critical fluid case also shows earlier happening vortex pairing process, indicating the less stable characteristic than the ideal gas jet. Due to the low injection Mach number, the density variation induced by the pressure change is ignorable, and the temperature variance has dominant effect on the density variation. This is illustrated by the similarity between the density distribution and the temperature distribution. The pressure field is compatible to the vorticity field. The density gradient field exhibits that the near-critical fluid case has sharper density stratification than the ideal gas case. The reason is that the vanishing thermal diffusion coefficient of near-critical fluids hinders the thermal diffusion and causes the larger temperature gradient between jet and ambient fluids which leads to the larger density stratification. Moreover, the larger density variation in the near-critical fluid mentioned above also contributes to the stronger density stratification.

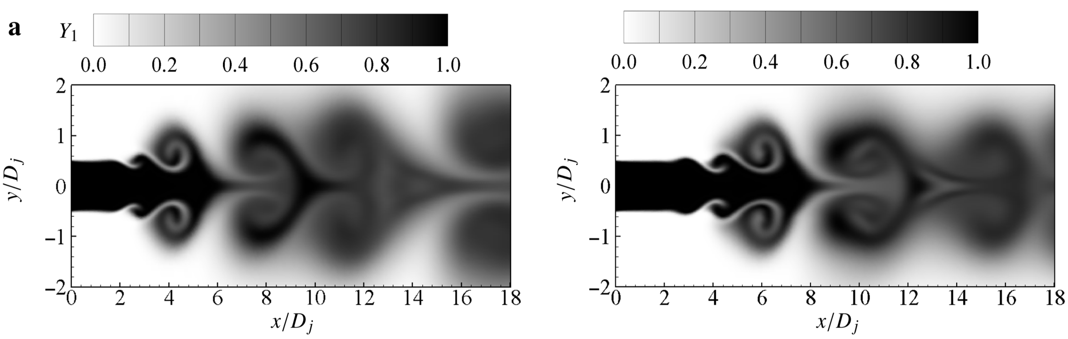

Fig. 3 Instantaneous flow fields of Near-critical fluid jet with $T_j = T_{\rm cr}+0.1$ K, $T_\infty = T_{\rm cr}+0.1$ K (left column) and Ideal gas jet with $T_j = 500$ K, $T_\infty = 500$ K (right column), $p = p_{\rm cr}$, $Re_j = 1\,750$. **a** Scalar Y_1; **b** Vorticity magnitude $|\omega|$(s^{-1}); **c** Density ρ (kg$\cdot$m^{-3}); **d** Temperature T (K); **e** Density gradient magnitude $|\nabla\rho|$ (kg$\cdot$m^{-4}); **f** Gauge pressure p' (Pa)

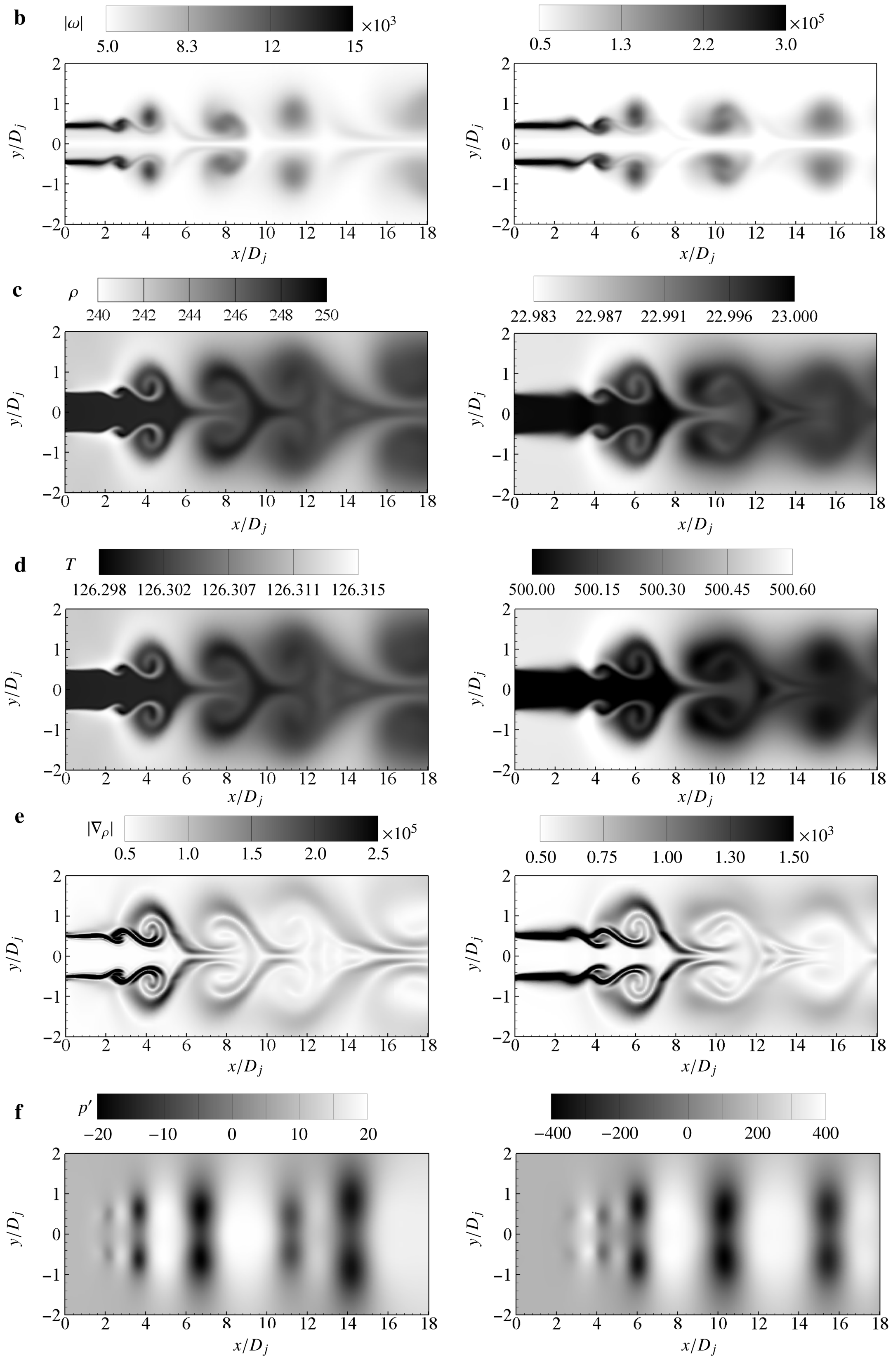

Fig. 3 Instantaneous flow fields of Near-critical fluid jet with $T_j = T_{cr} + 0.1$ K, $T_\infty = T_{cr} + 0.1$ K (left column) and Ideal gas jet with $T_j = 500$ K, $T_\infty = 500$ K (right column), $p = p_{cr}$, $Re_j = 1\,750$. **a** Scalar Y_1; **b** Vorticity magnitude $|\omega|(\mathrm{s}^{-1})$; **c** Density ρ ($\mathrm{kg \cdot m^{-3}}$); **d** Temperature T (K); **e** Density gradient magnitude $|\nabla\rho|$ ($\mathrm{kg \cdot m^{-4}}$); **f** Gauge pressure p' (Pa) (continued)

To quantitatively investigate the flow structure, the analysis by means of the power spectral density (PSD) and proper orthogonal decomposition (POD) was also conducted here. Figure 4 shows the PSD of the dimensionless transverse velocity component v at different positions along the shear layer (i.e. $x = 2D_j, 3D_j, 5D_j, 8D_j, 15D_j, 25D_j, y = 0.5D_j$). The PSD amplitude of the near-critical fluid case is larger than the ideal gas case, indicating more vigorous velocity fluctuations in the near-critical fluid case. As shown in Fig. 3, the shear layer is relatively flat and no obvious vortex structures occur at $x = 2D_j$. The dominant frequency at $x = 2D_j$ corresponds to the most unstable mode of the shear layer instability. At $x = 3D_j$ for the near-critical fluid jet, the subharmonic frequency at $x = 2D_j$ becomes dominant while the obvious change in the PSD of ideal gas jet is that the amplitude becomes larger. From Fig. 3, it is identified that the first vortex pairing in the near-critical fluid happens at $x = 3D_j$, indicating that the half dominant frequency at this position is caused by the vortex pairing process. For the ideal gas jet, the vortex rolling-up process starts around $x = 3D_j$ and the dominant frequency is the same as one at $x = D_j$, indicating that the vortex rolls up with the fundamental frequency of the shear layer instability. At $x = 5D_j$ for the near-critical fluid case, the PSD amplitude corresponding to the frequency 256 Hz becomes larger and the peak value corresponding to 523 Hz becomes smaller than that at $x = 3D_j$. This indicates that the first vortex pairing process continues at this position, two small vortices continue to form a larger vortex. For the ideal gas jet, the second dominant frequency 3 510 Hz appears. This indicates the first vortex pairing happens at this position. At $x = 8D_j$ the frequency corresponding to the first vortex pairing becomes dominant for both the near-critical fluid jet and ideal gas jet. At $x = 15D_j$, the dominant frequency of the near-critical fluid jet halves again, indicating the second vortex pairing happening. The dominant frequency of the ideal gas case still corresponds to the first vortex paring. At $x = 25D_j$, the dominant frequency corresponding to the second vortex pairing is identified in both the cases. The vortex rolling-up, the first and second vortex paring process in the ideal gas case occurs later than in the near-critical fluid case. The near-critical fluid jet is more unstable and develops faster than the ideal gas jet.

The POD analysis is commonly used for extracting energetic coherent structures from data. The POD of the velocity field was conducted in a $5D_j \times 25D_j$ near-field area. Figures 5–8 show the energy distribution and the spectra of the main POD modes of near-critical fluid case and ideal gas case, respectively. The first two modes contain most of the energy of the flow field. In comparison with Figs. 6 and 8, it is noticed that the vorticity distribution corresponding to the dominant POD modes of the near-critical fluid are remarkably different from that in ideal gas case. Combining the POD results with the above PSD analysis, it is found that the first two POD modes correspond to the vortex formed through pairing process. For near-critical fluid jet, the first mode containing most of the energy corresponds to the second vortex pairing,

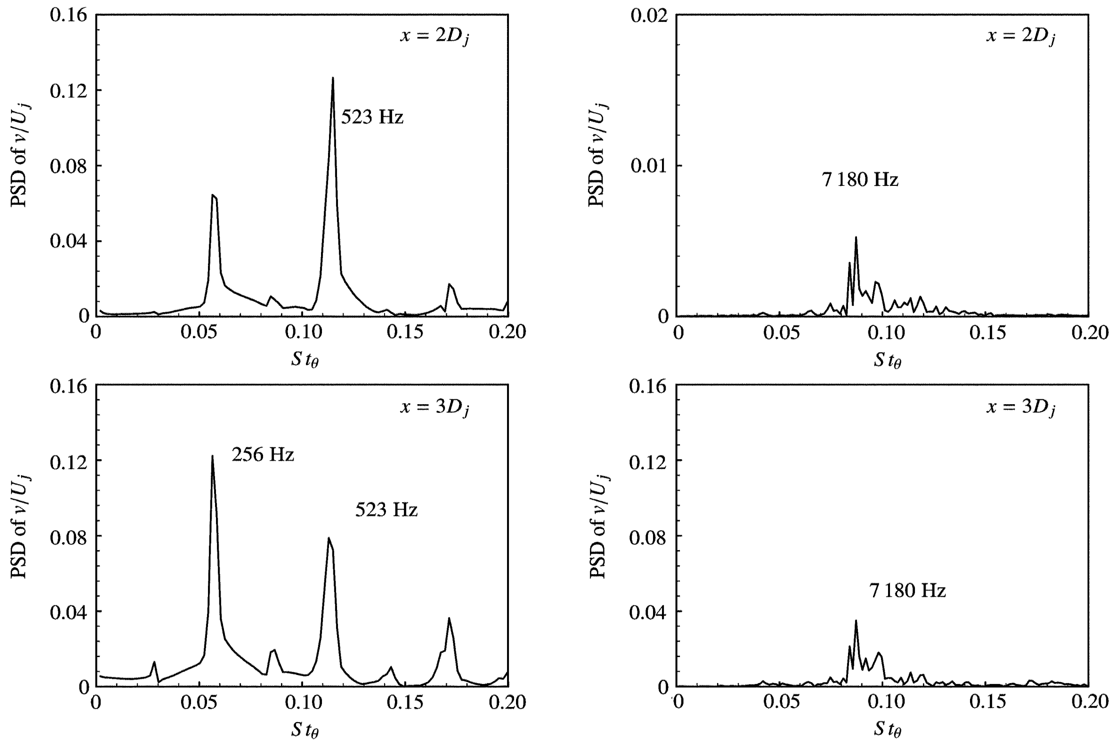

Fig. 4 PSD of normalized transverse velocity component v at different positions along the shear layer at streamwise direction ($x = x_i$, $y = 0.5D_j$): near-critical fluid case (left column), ideal gas case (right column)

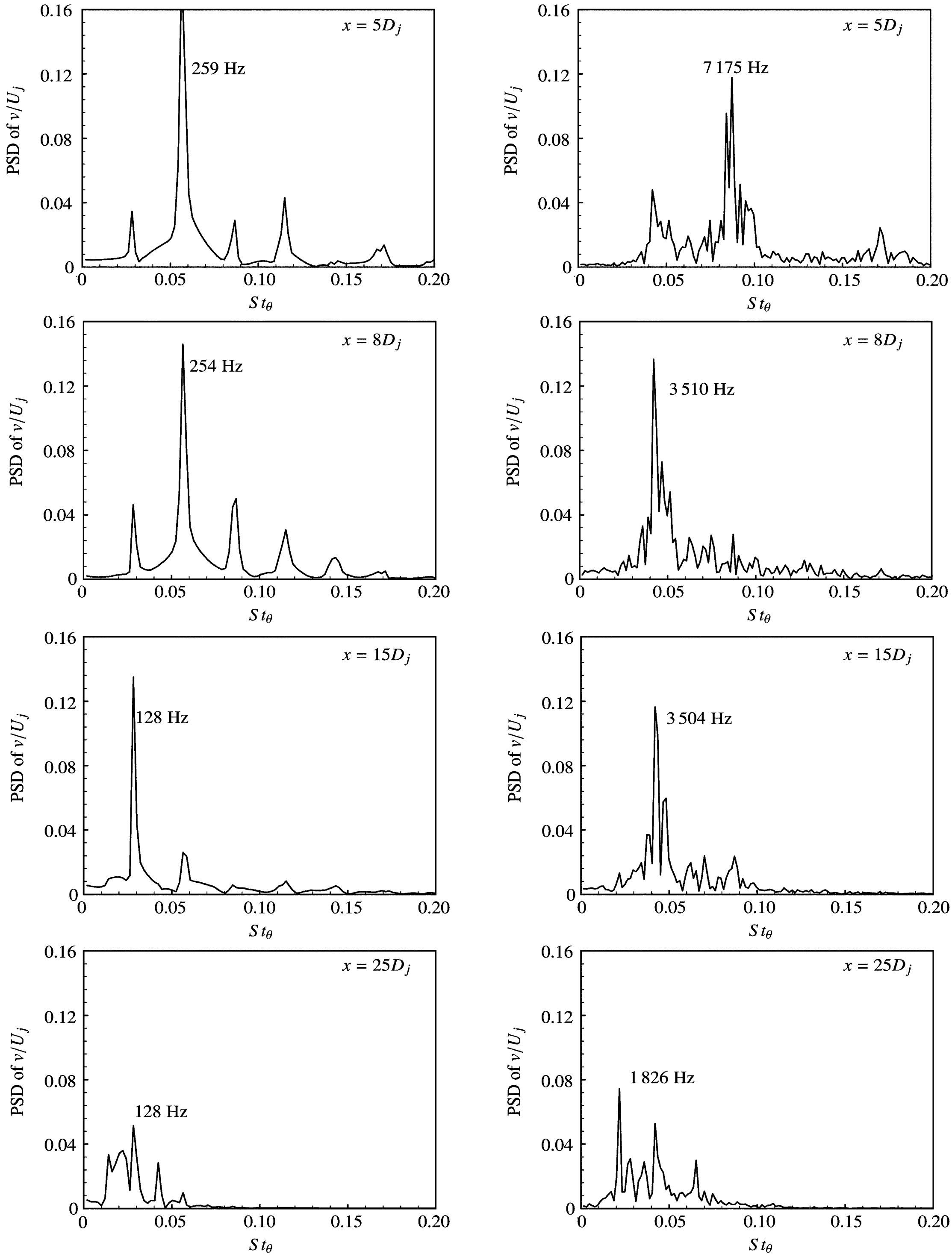

Fig. 4 PSD of normalized transverse velocity component v at different positions along the shear layer at streamwise direction ($x = x_i,\ y = 0.5D_j$): near-critical fluid case (left column), ideal gas case (right column) (continued)

while for the ideal gas jet it corresponds to the first vortex pairing. This indicates that the vortex formed through second vortex pairing is dominant in the near-critical fluid jet while the vortex formed through first vortex pairing is dominant for the ideal gas jet. This also presents faster developing and better mixing of the near-critical fluid case.

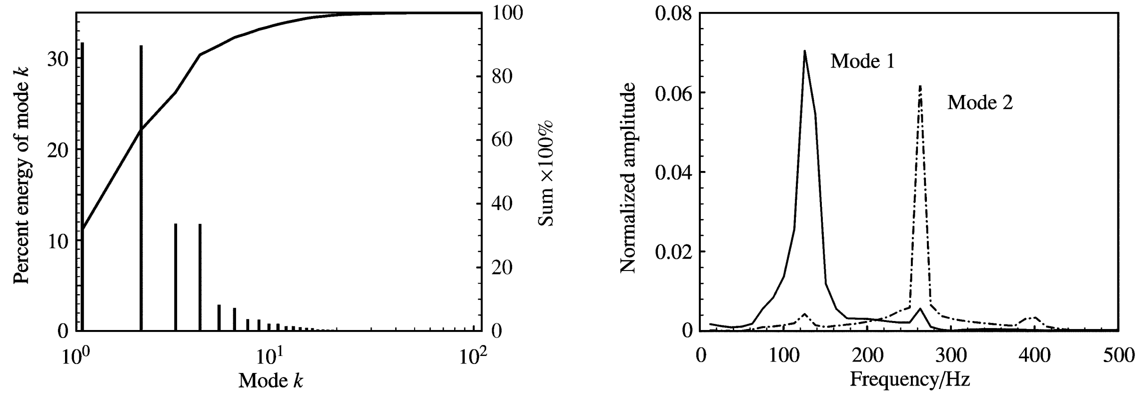

Fig. 5 Energy distribution (left) and spectra of time traces (right) of main POD modes of near-critical fluid jet

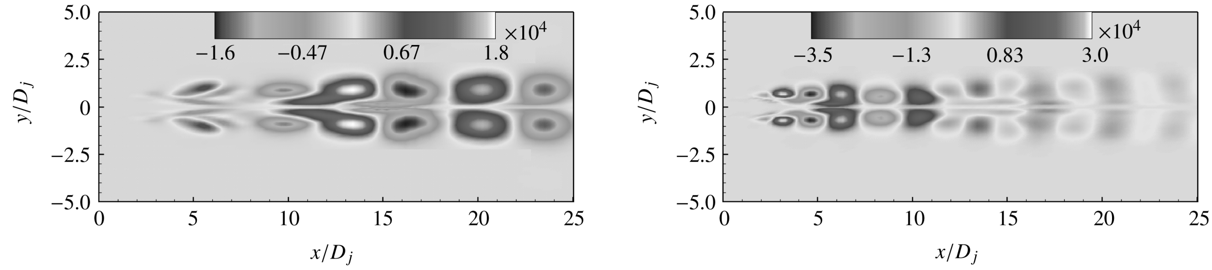

Fig. 6 Vorticity distribution corresponding to Mode 1 (left) and Mode 2 (right) of near-critical fluid case

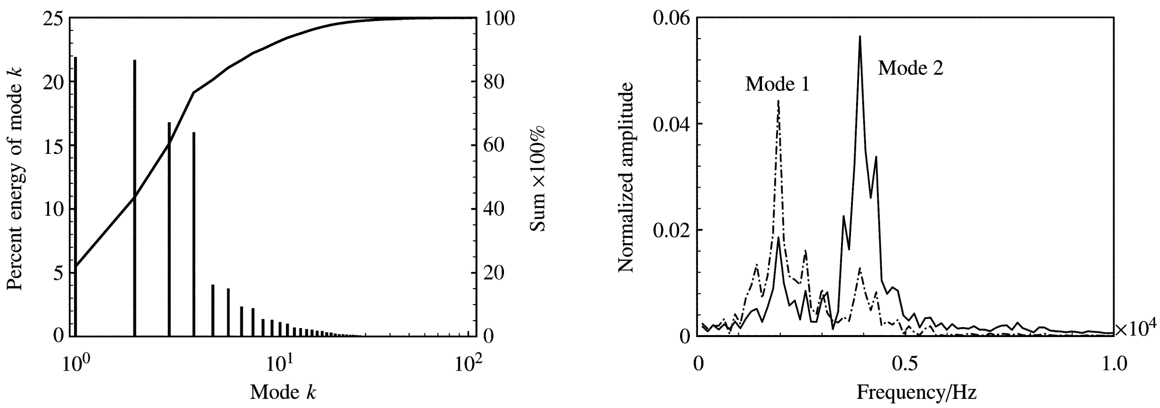

Fig. 7 Energy distribution (left) and spectra (right) of time traces of main POD modes of ideal gas case

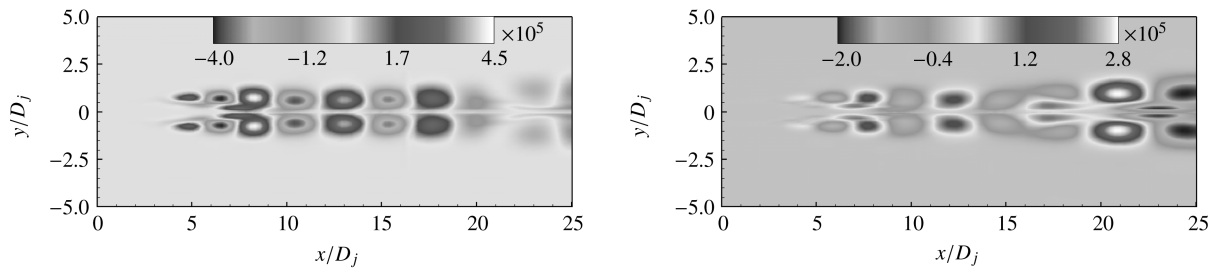

Fig. 8 Vorticity distribution corresponding to Mode 1 (left) and Mode 2 (right) of ideal gas case

5.2 Mean flow properties

The mean flow properties are obtained through time averaging after the flow field has reached its stationary state. Figure 9a shows the half-width $r_{1/2}$ of the mean streamwise velocity profile along the transverse direction, where the mean streamwise velocity is one half of its maximum value. As the jet developed to the downstream, it mixes with the ambient fluid and spreads in the transverse direction, and the half width becomes larger. Compared to the ideal gas jet, the near-critical fluid jet has larger half width at the same streamwise position, i.e. The indicates the near-critical fluid jet has larger spreading rate and spreading angle. Figure 9b shows the profile of the normalized mean temperature distribution $(T_c - T_j)/\Delta T$ along the center line in the streamwise direction, where the subscript "c" refers to the quantities at the jet center line, and ΔT is the maximum value of temperature variation in the chamber. The near-critical fluid jet has shorter potential core than the ideal gas jet. The larger slope of the temperature distribution following the core region in the near-critical fluid jet indicates its faster increasing temperature and better mixing with the abient fluid. Figure 10 shows the time averaged streamwise velocity profile along the transverse direction of the jet at different streamwise positions. No exact self-similar region was observed for either near-critical fluid jet or ideal gas jet. This is reasonable considering the laminar characteristic of the jet and the confining effect of the chamber. However, the normalized velocity profiles still show the trend that the near-critical fluid jet can achieve a quasi-self-similar region earlier than the ideal gas jet. The comparison of time averaged quantities demonstrates that the near-critical fluid jet spreads faster and mixes better with the ambient fluid than the ideal gas jet.

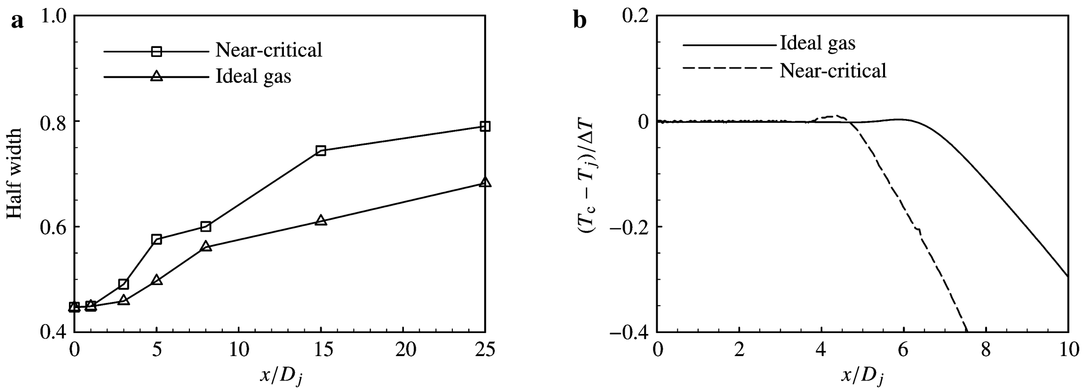

Fig. 9 Comparison of **a** half width and **b** potential core length between near-critical fluid jet and ideal gas jet

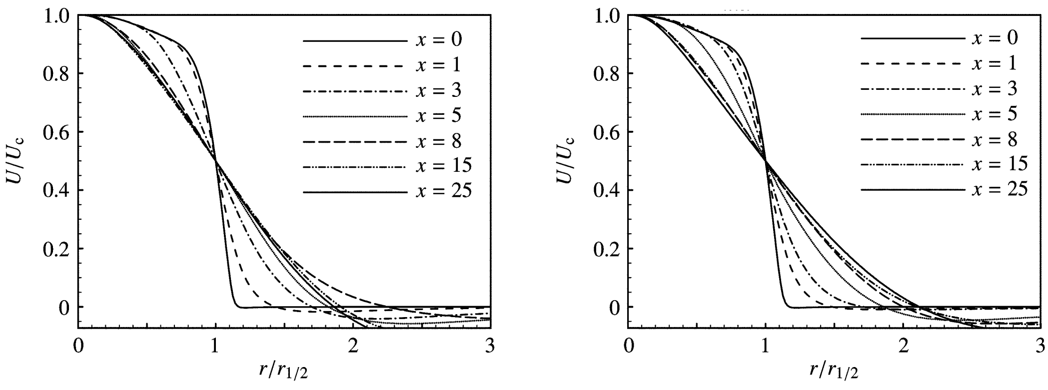

Fig. 10 Time averaged stream-wise velocity profile along y-direction: near-critical fluid case (left); ideal gas case (right)

5.3 Shear layer instability and vortical dynamics

To explain the faster development of the near-critical jet as compared with the ideal gas jet, further analysis at two different positions is conducted. The first position is the shear layer region without vortex rolling up in the near-field of the injector and the second position is the well developed vortex region at the downstream.

The dominant frequency of the shear layer instability is 523 Hz in the near-critical fluid case and 7 180 Hz in the ideal gas case. In the idea gas case, the dominant frequency gives a value of 0.088 for the Strouhal number $St = 2\pi f\theta/u_j$, where f is frequency and θ is momentum thickness. This value is consistent with Freymuth's result [31] for the natural oscillating frequency of a laminar constant density shear layer. In the near-critical fluid case, the Strouhal number is 0.1, which is higher than the ideal gas case. It is well known that large density stratification around the shear layer has a stabilization effect for high density jet. Usually the jet with higher density stratification has lower frequency oscillating shear layer. However, the shear layer with larger density stratification in the near-critical fluid is more unstable than that in the ideal gas. To explain this reason, some important factors in near-critical fluid flow, i.e. strong volume dilatation and contraction effect, should be considered. Figure 11 shows the dimensionless density gradient amplitude $|\nabla\rho|/|\nabla\rho|_{\max}$, the volume expansion rate $\nabla \cdot u/(u_{\mathrm{c}}/D_j)$, velocity components u/u_{c}, v/u_{c}, vorticity $\omega/\omega_{\max}$ and scalar Y_1 along the transverse direction of jet at $x = 1.5D_j$, where subscript "c" is the quantities at the center line of the jet, and "max" the maximum value alone the transverse direction at $x = x_0$. At $x = 1.5D_j$ there is no vortex structure formed and the shear layer remains flat. The profile of the normalized streamwise velocity, vorticity and mass fraction from the two cases are almost similar with each other. The density stratification of the near-critical fluid jet is much sharper than the ideal gas case due to small thermal diffusivity and large volume expansion coefficient as mentioned above. The volume dilatation and contraction of the near-critical fluid case near the shear layer is much stronger than the ideal gas case. As a result, the transverse velocity component v is much larger in the near-critical fluid case, indicating that more unstable shear layers exists and further leads to faster spreading jet.

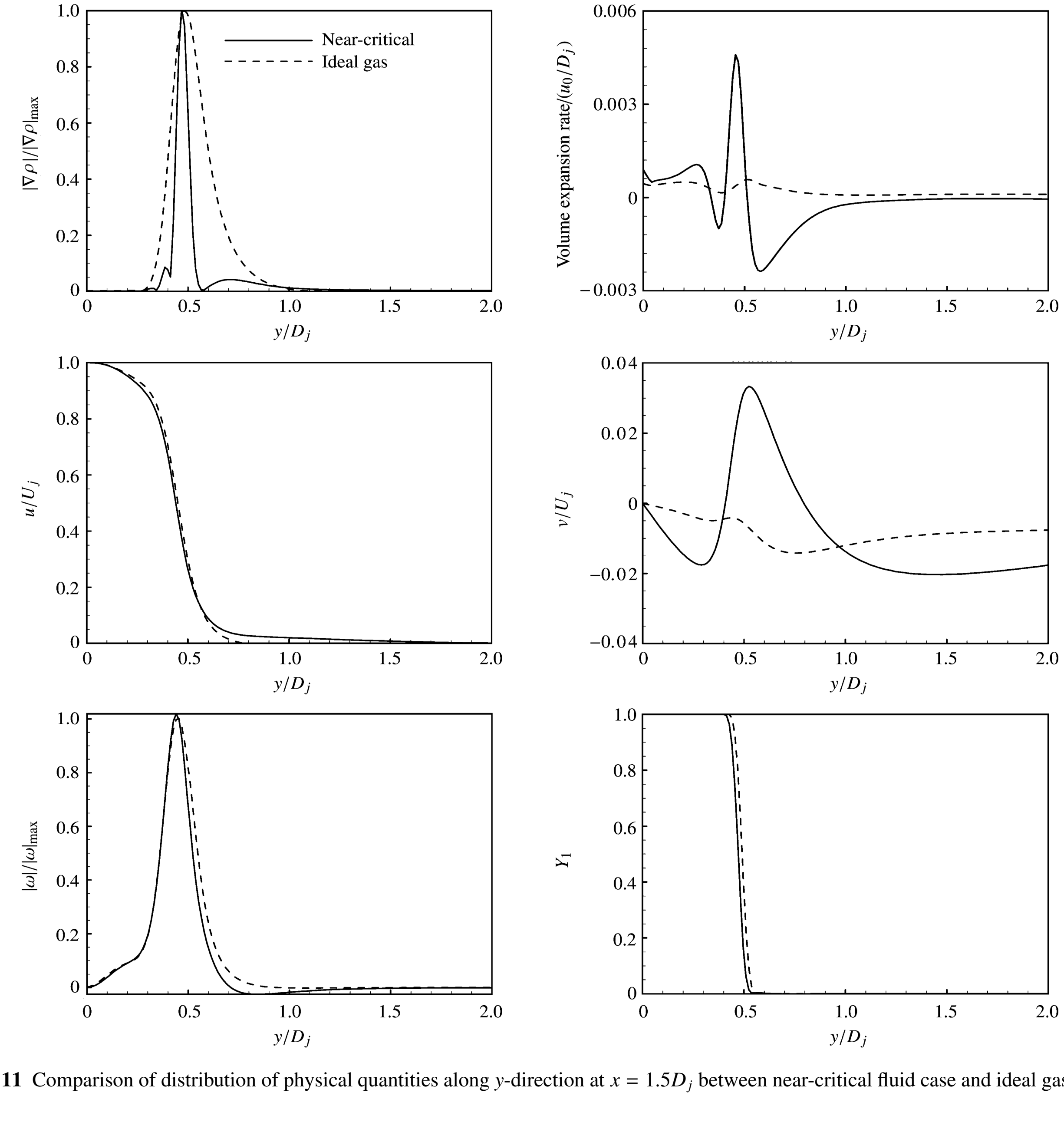

Fig. 11 Comparison of distribution of physical quantities along y-direction at $x = 1.5D_j$ between near-critical fluid case and ideal gas case

The stronger shear layer formed between jet and the ambient flow tilted and developed to large-scale structures. The vorticity dynamics can be quantified through the vorticity transport equation. Figure 12 shows an instantaneous vorticity budget and vorticity distribution at $x = 8D_j$ where the large vortex structures are well developed for both the cases. The results are normalized by the bulk velocity u_j and injector width D_j. Three effects contribute to the vorticity dynamics, i.e. the volume-dilatation effect $-\omega\nabla \cdot u$, the baroclinic torque effect $(\nabla\rho\times\nabla p)/\rho^2$ and viscous dissipation effect $\nabla\times(\nabla\cdot\tau/\rho)$. The viscous dissipation effect has a dominant effect in the ideal gas case while the other two effects are ignorable compared to the former. In the near-critical fluid case, the viscous dissipation effect is still dominant, however, the volume dilatation and baroclinic torque effect cannot be ignored. The volume dilatation and baroclinic torque effect have an important influence on vorticity dynamics in near-critical fluid jet. The volume dilatation effect and baroclinic torque effect compete with the viscous effect and reach peak value at the vortex center where the vorticity achieves its maximum value, and thus strengthen vorticity and stimulate the vortex rolling up and pairing process. Thus, different vorticity dynamics mechanisms are another important reason for the faster development of the near-critical fluid jet than the ideal gas jet.

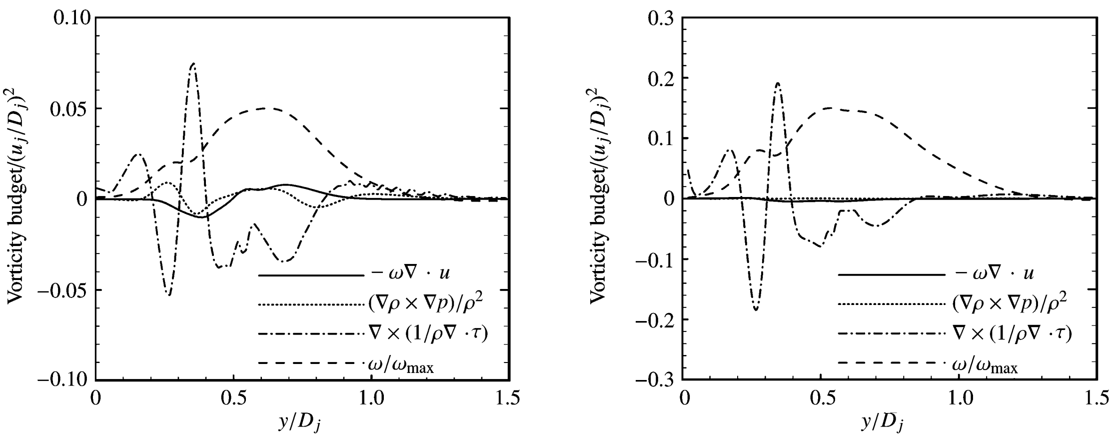

Fig. 12 Vorticity distribution and vorticity budget along y-direction at $x = 8D_j$: near-critical fluid case (left) and ideal gas case (right)

6 Concluding remarks

Nitrogen jet in the close vicinity of liquid-gas critical point is investigated. Comparison is made against an ideal gas jet with the same Reynolds number. The near-critical fluid jet has faster developed vortex rolling-up and pairing process than the ideal gas jet. Compared to the ideal gas case, the near-critical fluid jet has a larger spreading angle and shorter potential core. The near-critical fluid jet mixes more efficiently with its ambient fluid. Even though larger density stratification with stabilization effect exists in the near-critical fluid jet, stronger volume dilatation and contraction effect disturb the shear-layer, and make the near-critical fluid jet more unstable than the ideal gas case. Different vorticity dynamics mechanisms also exist in the two cases due to arising baroclinic effect and volume dilatation effect in the near-critical fluid case. These two effects are demonstrated to be another important reason for the faster developing behavior of the near-critical fluid jet.

References

1 Yang, V.: Modeling of supercritical vaporization, mixing, and combustion processes in liquid-fueled propulsion systems. Proc. Combust. Inst. **28**, 925–942 (2000)
2 Zappoli, B., Bailly, D., Garrabos, Y., et al.: Anomalous heat transport by the piston-effect in supercritical fluids under zero gravity. Phys. Rev. E **41**(4), 2264–2267 (1990)
3 Boukari, H., Shaumeyer, J. N., Briggs, M. E., et al.: Critical speeding up in pure fluids. Phys. Rev. A **41**(4), 2260–2263 (1990)
4 Onuki, A., Hao, H., Ferrell, R. A.: Fast adiabatic equilibration in a single-component fluid near the liquid-vapor critical point. Phys. Rev. A **41**(4), 2256–2259 (1990)
5 Wagner, H., Bayazitoglu, Y.: Thermal disturbances in near-critical fluids. J. Thermophys. Heat Transfer. **16**(2), 273–279 (2002)
6 Frohlich, T., Beysens, D., Garraabos, Y.: Piston-effect-induced thermal jets in near-critical fluids. Phys. Rev. E **74**(44), 046307-1-6 (2006)
7 Zappoli, B., Jounet, A., Amiroundine, S., et al.: Thermoacoustic heating and cooling in near-critical fluids in the presence of a thermal plume. J. Fluid Mech. **388**, 389–409 (1999)
8 Accary, G., Bontoux, P., Zappoli, B.: Convection in a supercritical fluid: a reduced model for geophysical flows. Phys. Fluids **19**, 014104-1-6 (2007).
9 Suresh, P. R., Srinivasan, K., Sundararajan, T., et al.: Reynolds number dependence of plane jet development in the transitional regime. Phys. Fluids **20**, 044105-1-12 (2008)
10 Klein, M., Sadiki, A., Janicka, J.: Investigation of the influence of the Reynolds number on a plane jet using direct numerical simulation. Int. J. Heat Fluid Flow **24**, 785–794 (2003)
11 Zong, N., Meng, H., Hsieh, S., et al.: A numerical study of

cryogenic fluid injection and mixing under supercritical conditions. Phys. Fluids **16**, 4248-4261 (2004)

12 Yu, M., Monkewitz, P. A.: Oscillations in the near field of a heated two-dimensional jet. J. Fluid Mech. **255**, 323–347 (1993)

13 Raynal, L., Harison, J. L., Favre-Marinet, M., et al.: The oscillatory instability of plane variable-density jets. Phys. Fluids **8**, 993–1006 (1996)

14 Newman, J. A., Brzustowski, T. A.: Behavior of a liquid jet near the thermodynamic critical region. AIAA J. **9**, 1595–1602 (1971)

15 Umemura, A., Wakashima, Y.: Atomization regimes of a round liquid jet with near-critical mixing surface at high pressure. Proc. Combust. Inst. **29**, 633–640 (2002)

16 Oschwald, M., Smith, J. J., Branam, R., et al.: Injection of fluid into supercritical environments. Combust. Sci. Tech. **178**, 49–100 (2006)

17 Chehroudi, B., Talley, D., Coy, E.: Visual characteristics and initial growth rates of round cryogenic jets at subscritical and supercritical pressures. Phys. Fluids **14**, 850–861 (2002)

18 Chehroudi, B., Davis, D.: The effects of pressure and acoustic field on a cryogenic coaxial jet. AIAA Paper 04-1330 (2004)

19 Okong'o, N. A., Bellan, J.: Direct numerical simulation of a transitional supercritical binary mixing layer: Heptane and nitrogen. J. Fluid Mech. **464**, 1–34 (2002)

20 Okong'o, N. A., Harstad, K. G., Bellan, J.: Direct numerical simulation of O2/H2 temporal mixing layers under supercritical conditions. AIAA J. **40**, 914–926 (2002)

21 Oefelein, J. C., Yang, V.: Modeling high-pressured mixing and combustion processes in liquid rocket engines. J. Propul. Power **114**, 843–857 (1998)

22 Oefelein, J. C.: Thermophysical characteristics shear coaxial LOX/H2 flames supercritical pressure. Proc. Combust. Inst. **30**, 2929–2937 (2005)

23 Zong, N., Yang, V.: Cryogenic fluid jets and mixing layers in transcritical and supercritical environments. Combust. Sci. Tech. **178**, 193–227 (2006)

24 Zong, N., Yang, V.: Near-field flow and flame dynamics of LOX/methane shear-coaxial injector under supercritical conditions. Proc. Combust. Inst. **31**, 2309–2317 (2007)

25 Jacobsen, R. T., Stewart, R. T.: Thermodynamic properties of nitrogen including liquid and vapor phase from 63K to 2000K with pressure to 10000 bar. J. Phys. Chem. Ref. Data **2**, 757–827 (1973)

26 Meng, H., Yang, V.: A unified treatment of general fluid thermodynamics and its application to a preconditioning scheme. J. Comput. Phys. **189**, 277–304 (2003)

27 Zong, N., Yang, V.: An efficient preconditioning scheme for real-fluid mixtures using primitive pressure-temperature variables. Int. J. Comput. Fluid Dyn. **21**, 217–230 (2007)

28 Hsieh, S. Y., Yang, V.: A preconditioning flux-difference scheme for chemically reacting flows at all mach numbers. Int. J. Comput. Fluid Dyn. **8**, 31–49 (1997)

29 Swanson, R. C., Turkel, E.: On central difference and upwind schemes. J. Comput. Phys. **101**, 292–306 (1992).

30 Li, H. G., Zong, N., Lu, X. Y., et al.: A consistent characteristic boundary condition for general fluid mixture and its implementation in a preconditioning scheme. Adv. Appl. Math. Mech. DOI:10.4208/ammm.11-m1160

31 Freymuth, P.: On transition in a separated laminar boundary layer. J. Fluid Mech. **25**, 683–706 (1966)